Contrasting Climate Responses to the Scattering and Absorbing Features of Anthropogenic Aerosol Forcings

ILISSA B. OCKO*

Program in Atmospheric and Oceanic Sciences, Princeton University, Princeton, New Jersey

V. RAMASWAMY AND YI MING

NOAA/Geophysical Fluid Dynamics Laboratory, Princeton, New Jersey

(Manuscript received 8 July 2013, in final form 1 April 2014)

ABSTRACT

Anthropogenic aerosols comprise optically scattering and absorbing particles, with the principal concentrations being in the Northern Hemisphere, yielding negative and positive global mean radiative forcings, respectively. Aerosols also influence cloud albedo, yielding additional negative radiative forcings. Climate responses to a comprehensive set of isolated aerosol forcing simulations are investigated in a coupled atmosphere–ocean framework, forced by preindustrial to present-day aerosol-induced radiative perturbations. Atmospheric and oceanic climate responses (including precipitation, atmospheric circulation, atmospheric and oceanic heat transport, sea surface temperature, and salinity) to negative and positive particulate forcings are consistently anticorrelated. The striking effects include distinct patterns of changes north and south of the equator that are governed by the sign of the aerosol forcing and its initiation of an interhemispheric forcing asymmetry. The presence of opposing signs of the forcings between the aerosol scatterers and absorbers, and the resulting contrast in climate responses, thus dilutes the individual effects of aerosol types on influencing global and regional climate conditions. The aerosol-induced changes in the variables also have a distinct fingerprint when compared to the responses of the more globally uniform and interhemispherically symmetric well-mixed greenhouse gas forcing. The significance of employing a full ocean model is demonstrated in this study by the ability to partition how individual aerosols influence atmospheric and oceanic conditions separately.

1. Introduction

Atmospheric concentrations of aerosols have risen considerably since the Industrial Revolution in the mid-nineteenth century resulting from a myriad of human activities mainly in the Northern Hemisphere (NH) (Solomon et al. 2007). In contrast to the primary absorption and emission of longwave radiation by greenhouse gases, aerosols mainly scatter and absorb shortwave (solar) radiation depending on the composition of the particle. This divergence in aerosol optical behavior, when considering the species individually, yields opposite signs of radiative forcing perturbations on the climate (e.g., Hansen et al. 1998; Forster et al. 2007; Ocko et al. 2012). Furthermore, because the majority of emission sources reside in the NH and aerosols have a short atmospheric lifetime (several days) before they are removed by dry or wet deposition, the uneven horizontal distributions of anthropogenic aerosols give rise to interhemispherically asymmetrical forcings.

Climate responses to aerosol radiative forcings have been studied using global climate models, although almost all studies either present responses to the net aerosol forcing (e.g., Feichter et al. 2004; Ming and Ramaswamy 2009; Bollasina et al. 2011; Friedman et al. 2013) or do not include both scattering and absorbing aerosol forcing agents (e.g., Taylor and Penner 1994; Wang 2004; Chung and Seinfeld 2005; Ramanathan and Carmichael 2008; Ming et al. 2010; Frieler et al. 2011; Hwang et al. 2013; Mahajan et al. 2013). Those studies that do isolate aerosol species primarily focus on temperature and precipitation responses (e.g., Takemura et al. 2005; Jones et al. 2007; Andrews et al. 2010). Studies show that the temperature

* Current affiliation: Environmental Defense Fund, New York, New York.

Corresponding author address: Ilissa B. Ocko, Environmental Defense Fund, 257 Park Avenue South, New York, NY 10010.
E-mail: iocko@edf.org

DOI: 10.1175/JCLI-D-13-00401.1

change induced by anthropogenic aerosol emissions is more pronounced in the NH than in the Southern Hemisphere (SH), but the peak forcing and temperature anomalies are not spatially correlated (Shindell et al. 2010). Studies have also found that aerosols decrease precipitation rates in the global mean, increase atmospheric stability, perturb tropical circulation, and have strong regional effects (e.g., Ramanathan et al. 2001; Wang 2004; Chung and Seinfeld 2005; Ming et al. 2010). Few studies have compared how positive and negative aerosol radiative forcings, and their interhemispheric asymmetry, affect key circulation variables [e.g., Yoshimori and Broccoli (2008), who examined streamfunction responses to a suite of isolated positive and negative forcings].

Further, to our knowledge, no earlier study has partitioned and discussed the atmospheric and oceanic responses due to aerosol perturbations using a full ocean model and analyzing on a global scale. While a significant majority of studies analyzing climate responses to aerosols use a slab ocean, recent studies are shifting toward employing a full ocean (e.g., Meehl et al. 2008; Ackerley et al. 2011; Bollasina et al. 2011; Rotstayn et al. 2012). However, these studies focus on regional, not global, effects, and few focus on the separate effects from individual scattering and absorbing aerosols.

In this study, we investigate global atmospheric, oceanic, and surface responses to individual aerosol forcing configurations, highlighting the mechanisms induced by positive and negative aerosol forcings. We use a coupled global climate model with a full ocean, in contrast to the majority of the earlier studies that employed a mixed-layer ocean in part to be computationally less expensive. We analyze global and zonal mean changes in several key climate variables (surface air temperature, precipitation, specific humidity, vertical velocity, atmospheric circulation, poleward heat transport, sea surface temperature, and salinity) between the preindustrial period and the present day. In doing so, we aim to understand how strong anthropogenic asymmetrical positive and negative aerosol radiative forcings contribute to climate changes in their intrinsic ways, and how they compare with one another. In addition, we compare the aerosol-induced effects with those due to well-mixed greenhouse gases. Earlier studies that explore similar responses by employing a mixed-layer ocean version of the coupled climate model used here (e.g., Yoshimori and Broccoli 2008; Ming and Ramaswamy 2011) are valuable for highlighting the importance of considering a full ocean model.

2. Model and experimental design

We employ the National Oceanic and Atmospheric Administration (NOAA) Geophysical Fluid Dynamics Laboratory (GFDL) coupled global climate model, version 2.1 (CM2.1), to evaluate changes in climate variables from 1861–80 (preindustrial) to 1981–2000 (present day) in the context of isolated forcings relevant for the aerosol species and the well-mixed greenhouse gases [referred to in this study as long-lived greenhouse gases (LLGHGs)]. CM2.1 contains reasonable aerosol distributions compared to observations and a notably successful reproduction of twentieth-century temperatures (Ginoux et al. 2006; Delworth et al. 2006; Knutson et al. 2006). CM2.1 is evaluated as one of the most successful climate models in phase 3 of the Coupled Model Intercomparison Project (CMIP3) by the climate metric examination in Reichler and Kim (2008). Comparisons of the standard all-forcing results of surface temperature changes with observations are discussed in Knutson et al. (2006).

The model couples four components—atmosphere, land, ocean, and sea ice. A full description of the model is found in Delworth et al. (2006). The atmospheric component has a horizontal resolution of 2° (latitude) by 2.5° (longitude), with 24 vertical levels. The land component has the same horizontal resolution as the atmosphere. The ocean resolution is 1° by 1°, with finer meridional resolution equatorward of 30°, and 50 vertical levels. The sea ice component contains three vertical levels, one as snow and two as ice (Hunke and Dukowicz 1997; Winton 2000). There are three thickness categories for the layers. The ocean and sea ice models contain a tripolar grid with poles over North America, Eurasia, and Antarctica to avoid polar filtering in the Arctic. Initial conditions for the model are outlined in Stouffer et al. (2004) and contain a multicentury spinup prior to the model start time at 1861. The four model components interact via flux exchanges every 2 h, using a flux coupler module.

Aerosol emissions are based on several inventories used in the Intergovernmental Panel on Climate Change Fourth Assessment Report (IPCC AR4; Olivier et al. 1996; Cooke et al. 1999; van Aardenne et al. 2001); specific details and assumptions are outlined in Horowitz (2006). Atmospheric distributions of aerosols are simulated offline using a chemistry transport model, the Model for Ozone and Related Chemical Tracers, version 2 (MOZART-2; Tie et al. 2005; Horowitz 2006); aerosol concentrations in the atmosphere are governed by emissions, chemical transformations, transport (advection, diffusion, and convection), and wet and dry deposition. Aerosol three-dimensional concentration fields are then fed into CM2.1 as input.

CM2.1 calculates the aerosol optical and radiative properties online. Aerosol optical properties are derived from Mie theory (Haywood and Ramaswamy 1998), and sulfate particles grow hygroscopically as ammonium sulfate (Tang and Munkelwitz 1994). Atmospheric radiation

TABLE 1. Description and acronym of the experiments simulated with CM2.1 for the anthropogenic climate forcing from PI to PD. One case (AIE) is derived from other integrations as indicated.

Experiment	Description	Acronym
All-forcing	Standard all-forcing run including anthropogenic (long-lived greenhouse gases, stratospheric ozone, tropospheric ozone, aerosol direct radiative forcings, and land surface), and natural (volcano and solar) forcings.	AF
Long-lived greenhouse gases	Only anthropogenic long-lived greenhouse gases (carbon dioxide, methane, nitrous oxide, and halocarbons) are allowed to evolve over time.	LLGHG
Aerosol direct radiative forcing	Only the anthropogenic aerosol direct radiative forcings by anthropogenic sulfate, black carbon, and organic carbon are allowed to evolve over time.	AER
Sulfate	Only anthropogenic sulfate is allowed to evolve over time.	SUL
Black carbon	Only anthropogenic black carbon is allowed to evolve over time.	BC
Organic carbon	Only anthropogenic organic carbon is allowed to evolve over time.	OC
Low black carbon	Same as BC, except all black carbon above 750 mb (~18 km) is moved to 950 mb (~3.5 km).	BCL
All-forcing and aerosol indirect radiative forcing	Same as AF, except with aerosol indirect radiative forcings from cloud brightening.	AF_AIE
Aerosol indirect radiative forcing*	Residual responses from (AF_AIE) − (AF) to isolate aerosol indirect effects.	AIE

* Response scenario derived using a combination of integrations; these are not results from direct simulations with CM2.1.

calculations use the shortwave radiation algorithm of Freidenreich and Ramaswamy (1999) and longwave radiation algorithm of Schwarzkopf and Ramaswamy (1999). Specific details of modifications to these shortwave and longwave algorithms to enhance computational efficiency are described in Anderson et al. (2004). For the individual aerosol simulations, aerosols are externally mixed and comprised of the direct (and, implicitly, semidirect) effects. We also consider the aerosol first indirect effect (cloud–albedo effect) by adopting a cloud brightening algorithm (Ming et al. 2005) to represent the cloud albedo increase effect caused by pollution aerosols (e.g., Forster et al. 2007). We do not include black carbon deposition on snow and ice.

We employ CM2.1 to assess changes in key climate variables from 1861–80 [preindustrial (PI)] to 1981–2000 [present day (PD)] for the individual forcing cases described below and in Table 1, which includes aerosol species and LLGHGs and the evolution of their respective three-dimensional distributions with time. For each forcing case, the model is integrated for 140 years to obtain the corresponding climate response from PI to PD. A suite of eight forcing cases, characterized by the space–time evolution of the forcing agent, is employed in the model (Table 1), with the resulting model integrations enabling a platform to separate and evaluate the desired responses.

Forcing experiments comprise a standard all-forcing case (AF) [LLGHGs + stratospheric ozone + tropospheric ozone + aerosol direct radiative forcing (DRF) + land surface + volcanic + solar, and without the indirect effect from aerosols]; LLGHG-only; and several different anthropogenic aerosol configurations as explained below. All integrations (except one, as described below) consist of three ensemble members, each starting from different initial conditions of the coupled system (Stouffer et al. 2004). We note that, in the AF case, the land surface radiative forcing is $-0.04\,\mathrm{W\,m^{-2}}$ and solar radiative forcing is $0.3\,\mathrm{W\,m^{-2}}$ (Knutson et al. 2006). The AF forcing, which includes the LLGHG forcing, is approximately similar to the IPCC estimate (Solomon et al. 2007); however, some of the minor forcing contributors there are not considered here.

The anthropogenic aerosol scenarios comprise several forcings obtained by considering them explicitly in a preindustrial to present-day integration. These are all-aerosol DRF (AER) (sulfate + black carbon + organic carbon); sulfate DRF (SUL) (in terms of anthropogenic tropospheric emissions only and does not include volcanic sources); black carbon DRF (BC) (which implicitly includes the "semi-direct" effect; Solomon et al. 2007); and organic carbon DRF (OC). All global mean forcing estimates can be found in Table 2.

Sulfate, black carbon, and organic carbon top-of-the-atmosphere (TOA) DRFs and surface forcings are described in detail in Ocko et al. (2012); forcings are calculated using the standard IPCC definition in Solomon et al. (2007), as the instantaneous change in the net radiative flux at the tropopause between preindustrial and present-day aerosol concentrations with suppressed climate responses. Forcings account for simulated meteorological conditions, sulfate hygroscopicity (as ammonium

TABLE 2. Global mean top-of-the-atmosphere radiative forcings (RF) and climate responses from isolated forcing scenarios. Changes in surface air temperature (ΔSAT) and precipitation rate (ΔP) are computed as the difference between PI (1861–80) and PD (1981–2000) conditions. The hydrological sensitivity (ΔP divided by ΔSAT) is also shown. Uncertainties are calculated as the adjusted standard error accounting for temporal autocorrelation (and adjusted degrees of freedom) using a Student's t test. All differences are found to be significant ($p \ll 1$; 0.05) except for organic carbon ΔSAT and ΔP.

Forcing scenario	RF ($W m^{-2}$)	ΔSAT (K)	ΔP ($mm\ day^{-1}$)	ΔP (%)	$\Delta P/\Delta$SAT (% K^{-1})
Standard all-forcing	2.6	0.81 ± 0.054	0.00 ± 0.0033	—	—
LLGHG	2.3	0.90 ± 0.044	0.04 ± 0.0026	1.40	1.56
Aerosol DRF	−0.51	−0.15 ± 0.046	−0.04 ± 0.0041	−1.39	9.27
Sulfate	−1.1	−0.26 ± 0.029	−0.02 ± 0.0033	−0.61	2.35
Black carbon	0.86	0.23 ± 0.038	−0.01 ± 0.0028	−0.34	−1.48
Low black carbon	0.31	0.35 ± 0.025	0.01 ± 0.0024	0.25	0.71
Organic carbon	−0.27	−0.05 ± 0.030	0.00 ± 0.0023	—	—
Aerosol indirect RF	−2.4	−0.58 ± 0.087	−0.05 ± 0.0055	−1.48	2.55

sulfate), and external mixtures. For aerosol cases, this is virtually similar to the stratosphere-adjusted forcing result. Sulfate and black carbon represent the strongest scattering and absorbing anthropogenic aerosol species, respectively (CM2.1 TOA DRFs—SUL: $-1.12\ W m^{-2}$ and BC: $+0.86\ W m^{-2}$—are within the realm of previous estimates, but lie at the higher end of estimates in the literature). The net aerosol DRF is approximately similar to that reported in the Intergovernmental Panel on Climate Change (IPCC; Solomon et al. 2007) although the component values there and in the present case differ.

To assess the sensitivity of black carbon forcings to the vertical distribution, which is still poorly constrained (Koch et al. 2009), we simulate a case in which high-elevation black carbon concentrations are moved to a lower level in the atmosphere [i.e., "low" black carbon (BCL)], which, as we discuss later, yields an interesting contrast in the changes to precipitation. For similar distributions of black carbon but different concentrations, it has been shown that temperature and precipitation responses scale linearly (Mahajan et al. 2013).

An alternate all-forcing case included is the aerosol indirect effect (AIE) due to cloud brightening from sulfate serving as cloud condensation nuclei, integrated together with the AF, to yield a case (AF_AIE) that incorporates the so-called cloud albedo effects (Ming et al. 2005). This effect does not include other aerosol–cloud interactions, such as the aerosol effect on cloud lifetime (i.e., the second indirect effect). This alternate all-forcing case contains two ensemble members. To isolate the aerosol indirect effect mentioned above, AF is subtracted from AF_AIE neglecting any nonlinearities in the subtractions. The subtraction can be justified on two grounds. First, most of the nonlinearity comes from the high latitudes (Ming and Ramaswamy 2009). Nonlinearity does not apply as much for the tropical regions, and this is the region investigated the most in our study. Second, the lack of large temperature changes over the Southern Ocean, a characteristic of transient climate response, has the effect of suppressing nonlinearity at the SH high latitudes. The fact that the spatial pattern of the derived indirect forcing case resembles that of the sulfate case adds to our confidence in the validity of the subtraction method. This also provides a platform for examining a case of a strongly asymmetric negative aerosol forcing that is primarily located in the NH.

Climate responses are averaged over 1861–80 to represent PI climate, and over 1981–2000 to represent PD climate. The changes in key thermal and hydrological climate variables are tested for statistical significance using a Student's t test, accounting for temporal autocorrelation (Santer et al. 2000). The results are shown only for the global mean responses in Table 2, although the Student's t test was employed for the zonal mean responses as well; the majority of latitudinal bands had statistically significant climate responses for the strongest forcing cases (BC, SUL, LLGHGs, and AIE).

3. Results

We investigate how the isolated forcing scenarios influence the following climate variables: surface air temperature, precipitation rate, vertical velocity, specific humidity, atmospheric circulation (via the meridional mass streamfunction), atmospheric and oceanic heat transport (via the meridional mass fluxes), sea surface temperature, and salinity.

Whereas LLGHG forcings are ubiquitously positive and approximately interhemispherically symmetrical, climate responses to aerosol radiative forcings are driven by 1) a dependence on whether it arises from scattering (radiative cooling tendency) or absorption (radiative warming tendency), and 2) interhemispherically unequal aerosol loading arising from the dominance of aerosol emissions sources in the Northern Hemisphere (Fig. 1).

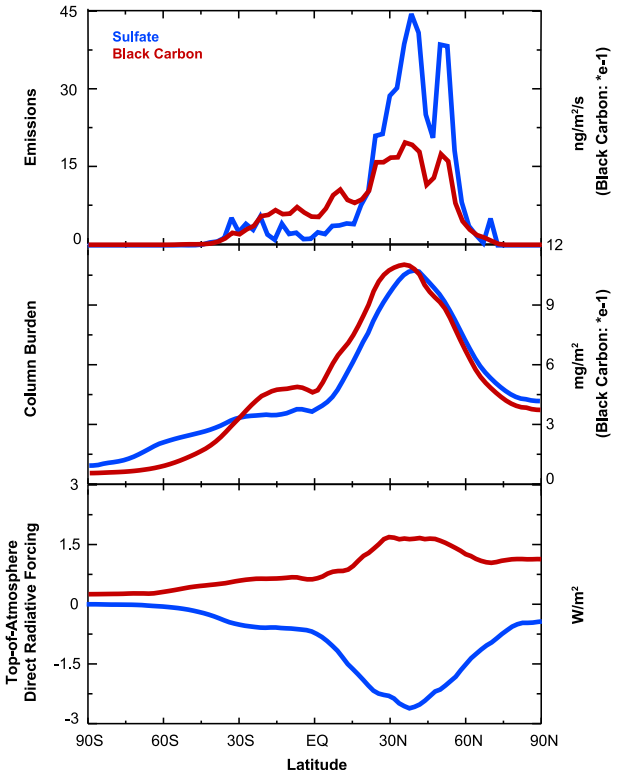

FIG. 1. Present-day (model year 2000) annual and zonal mean (top) emissions, (middle) burdens, and (bottom) TOA DRFs of sulfate and black carbon.

a. Global mean thermal and hydrological responses

Table 2 lists the global mean surface air temperature (ΔSAT) and precipitation (ΔP) changes for all of the forcing scenarios considered, along with global mean top-of-the-atmosphere radiative forcings (RF). For the AF and LLGHG cases, we compute the stratosphere-adjusted radiative forcing per Solomon et al. (2007), with our estimates reasonably similar to those in the IPCC. The global hydrological sensitivity (percent change in precipitation per kelvin) is also computed.

The sign of global mean ΔSAT for all configurations conforms to the sign of the forcing. For the AF scenario, a net positive forcing yields a warming response, and for the AER scenario (SUL + BC + OC), a net negative forcing yields a cooling response. Global mean temperature and precipitation responses for the OC forcing experiment are insignificant using a Student's t test, and therefore its quantitative aspects are mostly neglected in the analysis to follow, although their consistency with the relatively larger forcings offers a confirmation of the physics of the climate response.

The ΔSAT for AER is slightly more negative (−0.15 K) than, but close to, a linear summation of the individual responses to BC (0.23 K), SUL (−0.26 K), and OC (−0.05 K). Jones et al. (2007) also found a similarity in the temperature responses to aerosols added individually and taking the response to the combined aerosols' forcing. Both sulfate and black carbon aerosols yield a negative global mean change in precipitation from PI to PD despite the opposite temperature changes (discussed later.) Sulfate forcing decreases global precipitation by 0.61%, and black carbon forcing decreases global precipitation by 0.34%. Therefore, even though LLGHG ΔSAT is significantly stronger than that attributable to AER (aided by the partial canceling of opposing temperature responses from absorbing and scattering aerosols; OC contribution is statistically insignificant), the combined global mean ΔP from AER yields a response that is comparable in magnitude, but almost exactly opposite, to LLGHG (+1.40% for LLGHG and −1.39% for AER). This highlights that the combined nature of aerosol direct radiative effects on precipitation offsets the effects of the LLGHGs on global mean precipitation; this is to be contrasted with the aerosol species' tendency to offset one another in the thermal response. This latter factor dilutes the net aerosol effect vis-à-vis anthropogenic greenhouse gas emissions.

The cloud brightening effect (AIE) represents an even stronger influence of the scattering effects of aerosols through alteration of the cloud albedo. The albedo enhancement effect has a global temperature response that is slightly less than the LLGHG magnitude while, for precipitation, the response is slightly more. This highlights the importance of the aerosol-induced cloud albedo effect that, by itself, has the potential to rival the LLGHG forcing effects over the twentieth century, consistent with the forcing estimates presented by Forster et al. (2007). It is noted that the cloud albedo effect used in this model does not include other aerosol–cloud interactions, such as the aerosol second indirect effect (the effect on cloud lifetime; e.g., Lohmann and Feichter 2005; Ming and Ramaswamy 2009); further, the AIE forcing is on the upper end of estimates provided by the IPCC AR4 (Solomon et al. 2007) (Table 2).

The hydrological sensitivities vary across isolated forcing scenario, as noted by Frieler et al. (2011). Values are usually positive (more precipitation with warmer temperatures or less precipitation with cooler temperatures), largely owing to the balance that is necessary between the atmospheric longwave cooling (approximately proportional to the surface temperature) and latent heating (proportional to precipitation) (e.g., Ming et al. 2010). A notable exception is the case of black carbon. This arises from the complex relationship between black carbon and its effect on the hydrological cycle (e.g., Ming et al. 2010; Andrews et al. 2010). Black

carbon enhances the direct radiative heating of the atmosphere while warming the surface. The surface warming, from the atmospheric energy balance viewpoint, tends to increase the longwave cooling, and thus precipitation. The atmospheric absorption, however, has the effect of a decrease in precipitation under conditions of constant longwave cooling. Thus, the presence of black carbon exhibits opposing effects. In the BC experiment, the latter effect outweighs the former, resulting in a net decrease in the global mean precipitation.

Ming et al. (2010) demonstrate that the relative importance of the two factors affecting atmospheric stability and precipitation varies with the vertical profile of black carbon. In CM2.1, extensive vertical mixing from the chemistry transport model leads to high black carbon concentrations in the free troposphere, and thus a strong radiative forcing and atmospheric warming tendency. In our BCL experiment, however, the global mean precipitation response switches sign and becomes positive. This is because when the black carbon is close to the surface, the increased atmospheric absorption can be returned to the surface by adjusting the sensible heat flux exchange between the lowest atmospheric portion and the surface. Thus, the suppressing effect on precipitation is greatly diminished. This is why the global mean precipitation change becomes positive in BCL. This result highlights the fact that the vertical profile has an important bearing on the effect that black carbon brings in to the total aerosol effect, and to the degree it opposes or strengthens the sulfate-induced effects on precipitation (Ban-Weiss et al. 2012).

As already mentioned, the individual scattering (SUL) and absorbing (BC) aerosol global mean temperature responses roughly cancel but the precipitation responses do not. A small residual temperature response from the aerosol-only scenario AER, and a relatively stronger precipitation response for the same scenario, results in an extremely high hydrological sensitivity ($9.27\%\ K^{-1}$). Thus, the combined aerosol effect in global precipitation sensitivity would differ substantially from those of individual forcing components. However, this is different from aerosol effects on regional hydrological aspects as discussed below.

b. *Zonal mean thermal, hydrological, and dynamical responses*

Because aerosol forcings exhibit strong variability in their spatial distributions, it is more instructive to analyze zonal mean thermal, hydrological, and dynamical responses. For example, Fig. 1 shows the sulfate and black carbon annual and zonal mean emissions, burdens, and forcings in the present day, highlighting a strong asymmetry in hemispheric loading.

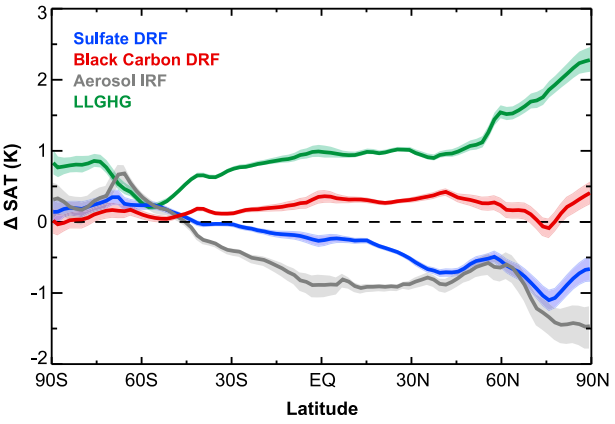

FIG. 2. Zonal mean surface air temperature responses from isolated forcing scenarios, computed as the difference between PI (1861–80) and PD (1981–2000) conditions. Shaded areas show the standard errors using a Student's *t* test.

For purposes of clarity, we focus only on four cases from the above. Specifically, we compare responses between 1) opposite forcings with similar spatial distributions (SUL versus BC responses) and 2) opposite forcings with different spatial patterns (asymmetrical AIE versus well-mixed LLGHG). These two pairings constitute examples that enable a study of comparisons and contrasts in climate responses involving the two central points of this study: positive and negative NH forcings, and interhemispheric asymmetry versus symmetry. We note that the zonal mean responses for the additional aerosol configurations (BCL and OC) are consistent with scenarios of the similar but stronger aerosol forcings.

1) SURFACE AIR TEMPERATURE

Figure 2 illustrates the zonal mean surface air temperature responses to SUL, BC, AIE, and LLGHGs from PI to PD. Zonal mean ΔSAT for all scenarios follow a familiar pattern, with amplification in the polar regions. The signs of the responses are generally consistent with the signs of the forcings, and scenarios with opposite forcings exhibit opposite temperature responses on average, more so in the NH. The temperature changes show a considerable interhemispheric temperature asymmetry, with stronger responses in the NH relative to the SH. An interhemispheric temperature asymmetry has been considered as an index of climate change, and is linked to changes in tropical precipitation and circulation patterns (e.g., Hwang et al. 2013; Chiang and Friedman 2012; Friedman et al. 2013).

Zonal mean patterns are generally consistent with Ramaswamy and Chen (1997), Stouffer et al. (1989), and Feichter et al. (2004). The relatively small temperature

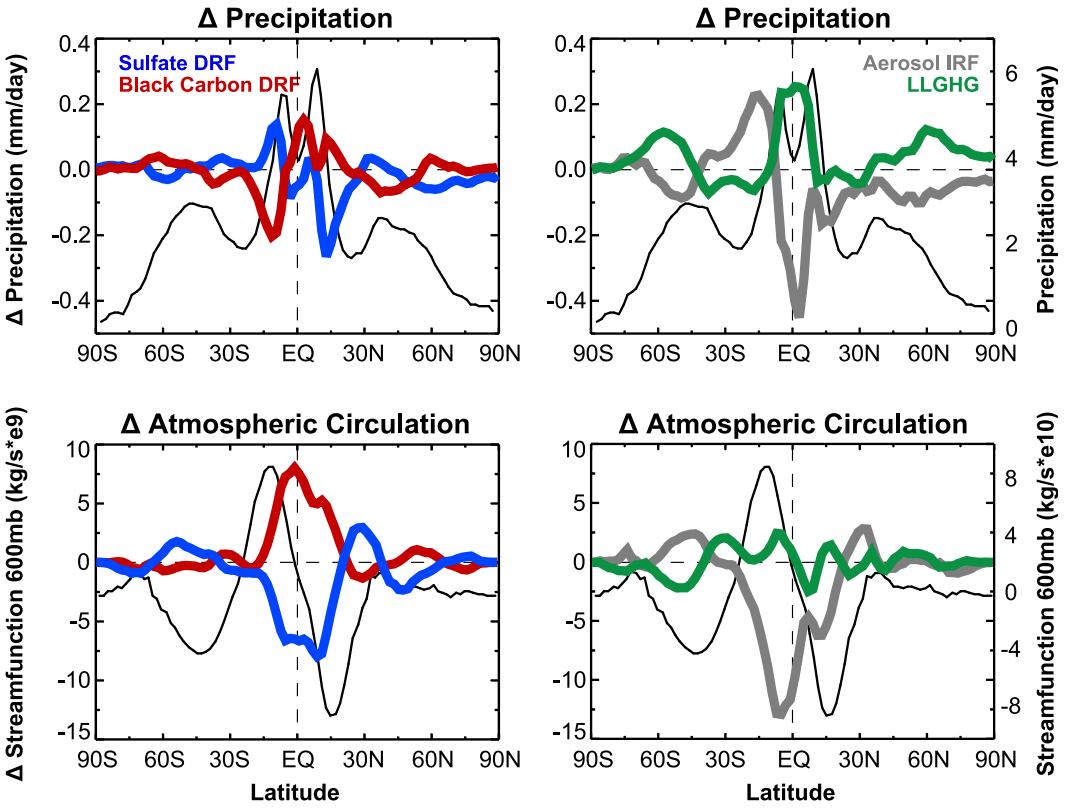

FIG. 3. Zonal mean responses in (top) precipitation and (bottom) meridional mass streamfunction at 600 mb (1 mb = 1 hPa) from isolated forcing scenarios, computed as the difference between PI (1861–80) and PD (1981–2000) conditions. PI zonally averaged annual mean fields are shown with the thin black curve with values on the right-hand axis. Meridional mass streamfunction is defined as the vertically integrated northward mass flux at each latitude from 600 mb to the TOA, where positive values indicate counterclockwise circulation.

responses south of 45°S are due to the damping effect of the Southern Ocean mixed layer, which is considerably deeper than other oceans (Manabe and Stouffer 2007). This explains why the magnitudes of the Southern Ocean responses simulated with a mixed layer ocean version of CM2.1 (Ming and Ramaswamy 2009) are much greater.

It is also interesting to note that the latitudes south of 45°S become warmer even in the negative radiative forcing cases (namely SUL and AIE). This is also found in the sea surface temperature responses discussed later in section 3c(1). Examination of individual ensemble members and statistical testing suggests that these features are likely robust. Possible explanations include that the combined ocean–atmosphere heat transport anomaly [discussed in section 3b(5)] warms the higher SH latitudes, or that weakening westerly winds over the Southern Ocean cause surface warming due to a reduced latent heat flux and subsequent wind stress–induced changes in ocean circulation [e.g., the opposite response to LLGHGs as shown in Lu and Zhao (2012)]. More research is needed to confidently assess the underlying cause.

Figures 3–6 illustrate the hydrological and dynamical responses to SUL, BC, AIE, and LLGHG forcings. The most striking features are the anticorrelations among the responses to cases with opposite forcings particularly in the lower latitudes (correlation coefficients provided in the subsequent sections for specified comparisons). For responses in precipitation, atmospheric circulation, vertical velocity, specific humidity, and heat transport, the locations of strong peak anomalies are at about the same latitudes, with a contrast in the signs, but with comparable magnitudes. This suggests that the meridional response patterns are strongly influenced by the forcing sign.

2) PRECIPITATION

The largest precipitation changes occur mostly around the equator (Fig. 3), consistent with previous studies [e.g., Held and Soden (2006) for the LLGHGs; see also Ming and Ramaswamy (2011)]. The latitudes of the strong precipitation anomalies align approximately with those of the vertical velocity anomalies (Fig. 4), such

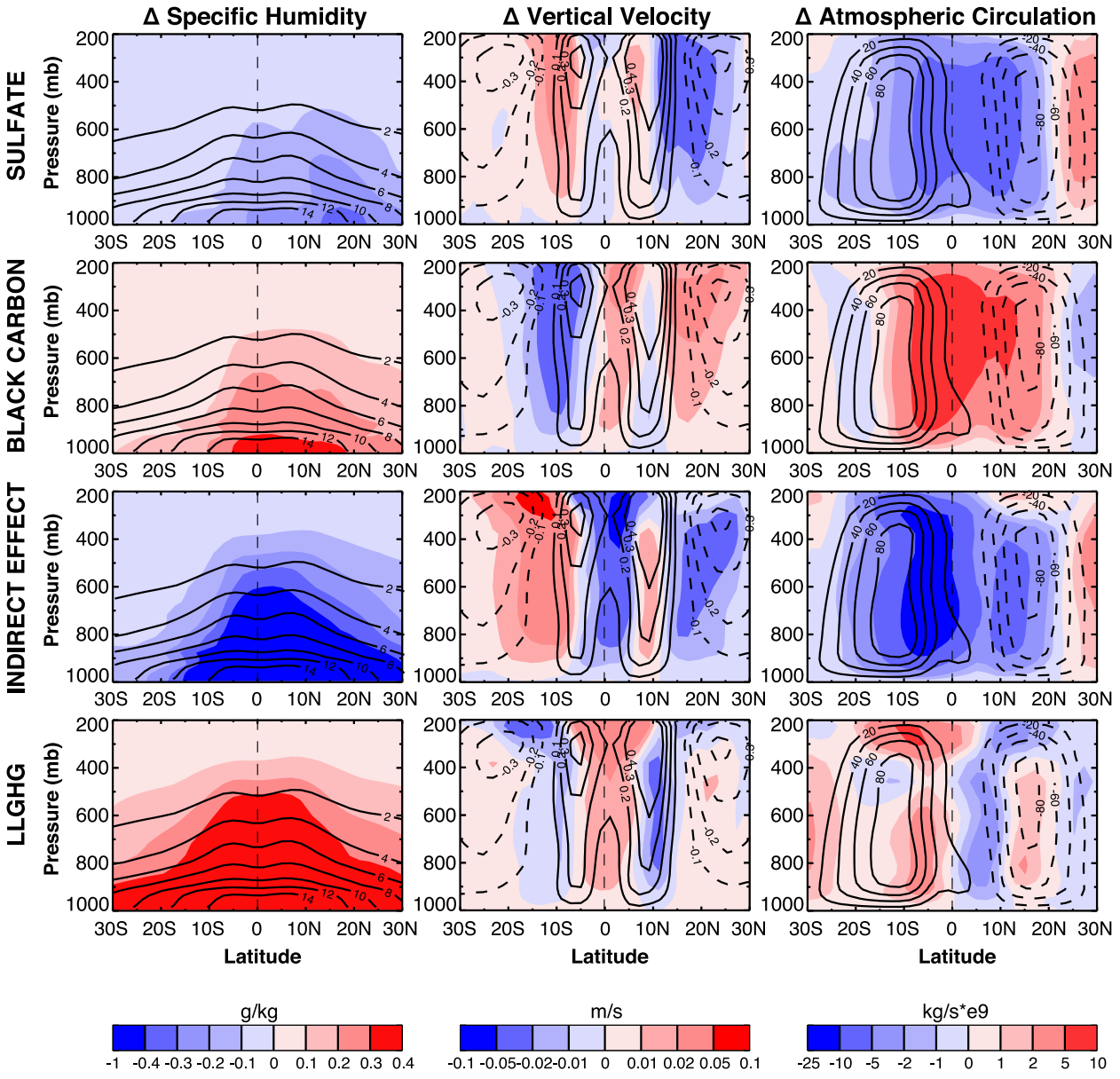

FIG. 4. Zonal mean responses in (left) specific humidity, (center) vertical velocity, and (right) meridional mass streamfunction from isolated forcing scenarios, computed as the difference between PI (1861–80) and PD (1981–2000) conditions. PI zonally integrated annual mean fields shown in overlying contours. Meridional mass streamfunction is defined as the vertically integrated northward mass flux at each latitude from the pressure level to the TOA, where positive values indicate counterclockwise circulation.

that strong increases (decreases) in precipitation are consistent with increases (decreases) in vertical velocity.

Both SUL and AIE ΔP (and vertical velocity) indicate a shift in the ITCZ southward, whereas BC ΔP indicates a shift in the ITCZ northward (Fig. 3). Forcings of smaller but similar magnitudes also follow suit. Because the majority of sulfur dioxide emitted and the resultant sulfate aerosols are in the NH, there is a heating differential created by a significant reduction in energy in the NH that is absent in SH. This reduces the diabatic heating in the NH, suppressing precipitation in the NH but enhancing precipitation in the SH from hemispheric continuity (e.g., Ramaswamy and Chen 1997). A recent multimodel assessment of precipitation responses to sulfate concludes that a shift in the ITCZ southward is found across nearly all CMIP3 and CMIP5 models (Hwang et al. 2013). AIE yields a similar, but enhanced, behavior, consistent with Rotstayn et al. (2000), Rotstayn and Lohmann (2002), Feichter et al. (2004), and Ming and Ramaswamy (2009).

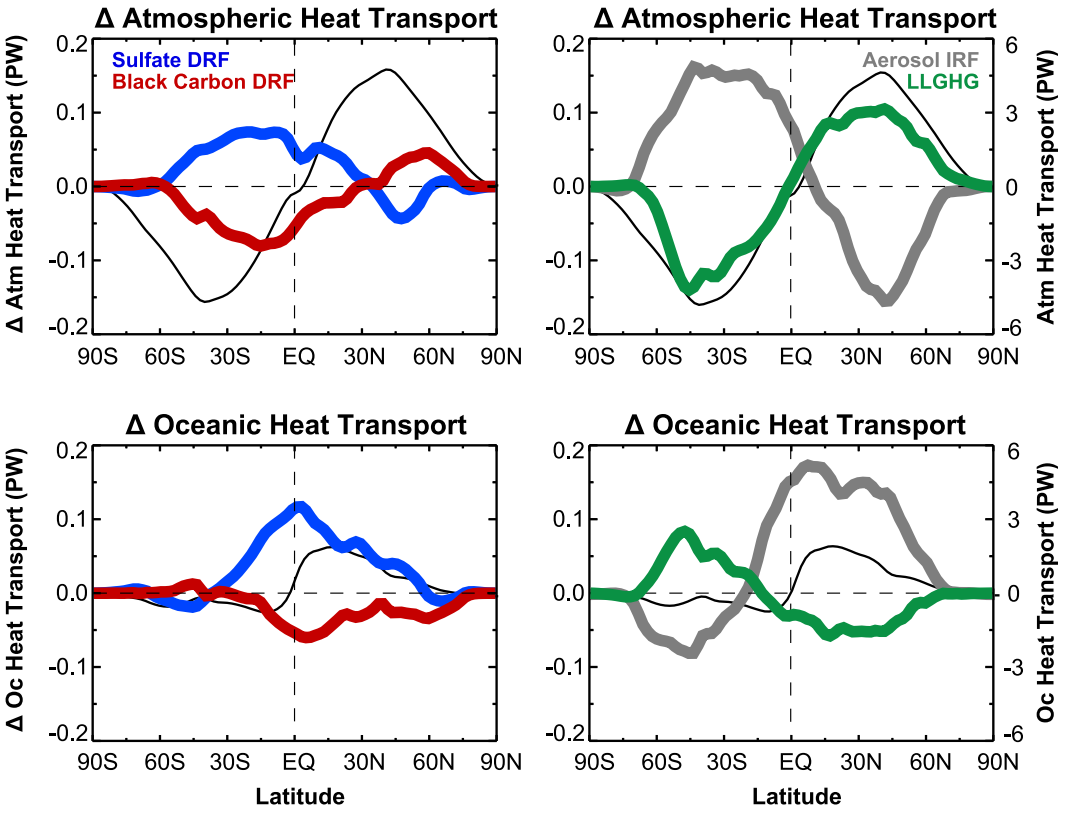

FIG. 5. Zonally integrated responses in (top) atmospheric and (bottom) oceanic heat transport from isolated forcing scenarios, computed as the difference between PI (1861–80) and PD (1981–2000) conditions. PI zonally integrated annual mean fields shown in thin black curve with values on the right-hand axis. Heat transport is defined as the meridional mass heat flux, where positive values indicate northward transport.

As discussed earlier, black carbon forcings affect precipitation in opposing ways in the global mean. However, black carbon suppression of precipitation, as a consequence of the radiative heating tendency of the atmosphere, is dominant. Hence both BC and SUL lead to lower global mean precipitation, albeit for different reasons. In the zonal mean, on the other hand, BC yields a fairly opposite precipitation response to SUL, especially prominent near the equator. This indicates that circulation changes in the two cases—which can be thought of, at least to the first order, as anticorrelated (r^2 = 0.85) [see section 3b(4)]—play a crucial role in determining the local precipitation responses. This result can also be found in Yoshimori and Broccoli (2008). Because the precipitation responses occur mostly around the equator—a region already under strong control of moist convection—it is likely that any effect on local stability due to black carbon's presence would be subtle. Erlick et al. (2006) suggest that in the case of shortwave absorbing aerosols, heating at the altitude of the low clouds enhances the convection in the tropics, leading to a decrease in atmospheric stability, whereas the midlatitudes are characterized by stronger stability and suppressed precipitation. Although our results show that black carbon shifts the ITCZ northward, the magnitude of increased precipitation in the NH is less than the magnitude of decreased precipitation by sulfate, despite similar surface air temperature responses of similar magnitude (Figs. 2 and 3).

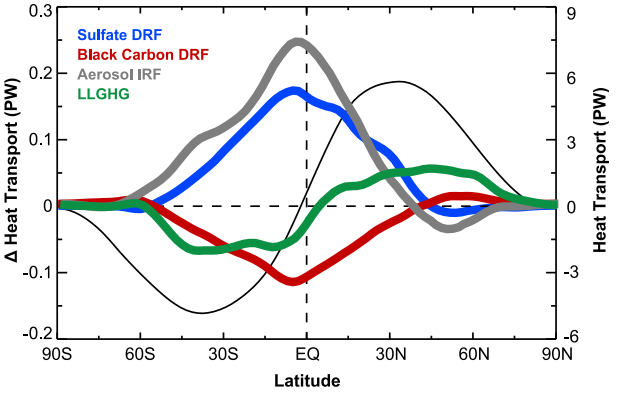

FIG. 6. As in Fig. 5, but for total heat transport.

Our BC results are in agreement with Chung et al. (2002), who found a substantial dynamical response in South Asia to absorbing aerosols, a northward shift of the ITCZ, enhanced precipitation in South Asia, and reduced precipitation elsewhere to compensate; and with Roberts and Jones (2004), Wang (2004), and Mahajan et al. (2013), who also found a northward shift of the ITCZ with a black carbon forcing. The BC zonal mean ΔP is also in agreement with Chung and Seinfeld (2005). Overall, the anticorrelated ΔP ($r^2 = 0.41$ in the tropics—from 30°S to 30°N) for SUL and BC [consistent with Yoshimori and Broccoli (2008)] highlights the significance of the sign of the forcing in governing the pattern of changes north and south of the equator, with consideration of the additional complexity arising from black carbon.

To assess the significance of the interhemispheric forcing asymmetry, we examine the response to the spatially uniform LLGHG forcing (Fig. 3). While the responses mainly occur around the equator as well, LLGHG ΔP is interhemispherically symmetrical [consistent with the mean climate and Held and Soden (2006)], in complete contrast to the aerosol forcing cases. While the LLGHG and AIE ΔP appear as anticorrelated ($r^2 = 0.52$), the strong dipole-like pattern of an increase in precipitation just south of the equator in the AIE case coupled with a decrease in precipitation south of the equator does not have a parallel in the LLGHG case, where the pattern is more symmetrical immediately about the equator. The interhemispheric asymmetry in ΔP for the AIE case with a dipole-like structure is approximately akin to the responses seen from the direct forcing by SUL and BC, with increases in precipitation in one hemisphere coupled with decreases in the other around the equator, therefore underscoring the significance of the interhemispheric forcing asymmetry in determining the equatorial precipitation responses.

3) Vertical velocity and specific humidity

Changes in vertical velocity and specific humidity in the tropics for the aerosol and LLGHG forcing scenarios are illustrated in Fig. 4. Vertical velocity responses are characterized by a multipole structure, with anomaly patterns that are mostly anticorrelated with comparable magnitudes for both forcing scenario pairings. The influence of interhemispheric asymmetry is still noticeable for the vertical velocity responses, but the influence of the sign of the forcing in governing anomaly patterns is most evident. It is clear, however, that both forcing sign and interhemispheric asymmetry influence the specific humidity responses. Negative forcings decrease specific humidity, and positive forcings increase specific humidity, consistent with the canonical climate model result that relative humidity is approximately constant in climate change scenarios (Held and Soden 2006). The specific humidity responses are practically mirror images between SUL and BC. Because of interhemispheric asymmetry, the aerosol configurations have responses that are skewed toward the NH, in contrast to LLGHG, which is symmetric about the equator.

4) Atmospheric circulation

Responses in the meridional atmospheric circulation yield quantitative insights into the significance of the sign of the forcing, and further amplify the inference concerning the interhemispheric forcing asymmetry (Figs. 3 and 4). SUL and BC forcings influence Hadley cell circulation in contrasting ways. SUL strengthens the ascending branch of the SH meridional mass circulation, and weakens the ascending branch of the NH meridional mass circulation. This is consistent with precipitation increases in the SH equatorial region, precipitation decreases in the NH, and a southward shift of the ITCZ. For BC forcings, on the other hand, the ascending branch in the NH is enhanced while the ascending branch in the SH is reduced. This is consistent with increased precipitation in the NH, decreased precipitation in the SH, and a northward shift of the ITCZ. These results are in agreement with Yoshimori and Broccoli (2008), and consistent with Hwang et al. (2013) for SUL and Roberts and Jones (2004), Wang (2004), and Chung and Seinfeld (2005) for BC. Furthermore, SUL forcing strengthens the Hadley cell circulation in the boreal winter, and weakens it during the boreal summer (not shown). BC forcing yields the opposite response: a stronger summertime circulation and a weaker wintertime circulation.

While there are cross-equatorial mirror patterns of tropical atmospheric circulation between scattering and absorbing aerosols ($r^2 = 0.85$), the well-mixed LLGHG forcing does not influence the circulation in nearly the same manner, or nearly as much, as all three aerosol configuration cases (Fig. 4), also seen in Yoshimori and Broccoli (2008) for carbon dioxide forcing. Circulation responses to aerosol forcings are therefore likely driven by the strong forcing asymmetry between the hemispheres, with the sign of the equatorial anomalies depending on the sign of the forcing. It is thus likely that the sign and magnitude of the temperature gradient between the NH and SH are governing the response, and are more germane than the identity of the forcing agent itself. Because this asymmetry is absent for LLGHG, the cross-equatorial circulation responses are not as strongly delineated. In summary, SUL and BC circulation responses are almost mirror opposites, and the LLGHG case shows little effect on the cross-equatorial circulation. For the responses shown in Fig. 4—specific humidity,

vertical velocity, and circulation—the AIE case is a stronger version of sulfate DRF responses in almost every respect [although there are some differences which are discussed in section 3b(5)], further suggesting the importance of the sign and magnitude of the spatial forcing.

5) HEAT TRANSPORT

Evaluation of the meridional heat [or moist static energy (MSE)] transport provides a quantification of the energetics of the response to aerosol forcings. The atmospheric and oceanic meridional fluxes are computed approximately by integrating the top-of-the-atmosphere and surface energy flux difference and the surface energy flux, respectively. Admittedly, this approach is less satisfactory for the ocean than for the atmosphere as the change in oceanic heat storage may not be negligible. Yet, as discussed later, it gives rise to results that are broadly consistent with those of Cai et al. (2006) and Cowan and Cai (2013) based on explicit flux calculation. This leads us to believe that our approach may be reasonably accurate. Note that the energy transport across the equator is in the direction of the upper branch of the Hadley cell because the MSE in the upper branch is higher than that in the lower branch (Held 2001; Hill et al. 2014).

Using a coupled global climate model enables separating of atmospheric and oceanic heat transport responses to aerosol forcings, an important aspect of their climate impact that has not been explored fully. The results are illustrated in Fig. 5, and indicate how the responses to forcings of different signs are generally opposite to each other. Positive forcing scenarios (BC and LLGHG) generally strengthen atmospheric poleward transport in each hemisphere, while negative forcing scenarios (SUL and AIE) generally weaken atmospheric poleward transport outside the tropics in each hemisphere. Ocean heat transport responses generally oppose those seen in the atmosphere for the AIE and LLGHGs, although this is less true for AIE because the transport is northward in the atmosphere and ocean in the SH tropics.

SUL and BC responses in the atmosphere and ocean are anticorrelated ($r^2 = 0.86$ for atmosphere and $r^2 = 0.68$ for ocean). A key difference between aerosol and LLGHG responses is that the aerosol cases exhibit a strong cross-equatorial heat flux, whereas the LLGHG case does not. For the aerosol cases, both the atmosphere and ocean transport heat across the equator in the same direction but with the aerosol forcing sign determining the direction. Therefore the net heat transport, shown in Fig. 6, shows a considerable cross-equatorial heat flux. The cross-equatorial heat fluxes are northward for negative aerosol forcings (redistributing heat to the NH where temperatures are reduced) and southward for positive aerosol forcings (redistributing excess heat to the SH). This is in agreement with the expectation that excess positive energy in one hemisphere drives energy transport to the other hemisphere, and is accompanied by a concurrent shift in the ITCZ toward the hemisphere with more positive energy as shown in Fig. 3 (Williams et al. 2001; Wang 2004; Kang et al. 2008; Frierson and Hwang 2012; Mahajan et al. 2013; Hwang et al. 2013).

The net heat transport response peaks in the tropics for the aerosol cases, as opposed to in the midlatitudes for LLGHGs [which follows the well-known meridional heat transport field shown in Fig. 6, also in Held and Soden (2006)]. While the negative AIE forcing also gives rise to northward cross-equatorial heat fluxes in both the atmosphere and ocean, the AIE and the SUL cases show notable differences at other latitudes; an example is the much stronger oceanic heat divergence poleward of 45°S in the AIE case. Furthermore, the aerosol DRF cases perturb heat transport in the atmosphere and ocean in similar ways, whereas this is not the case for the AIE scenario, where the oceanic heat transport response does not follow the atmospheric transport in terms of sign; in the SH, the ocean transports heat southward while the atmosphere transports heat northward. In the NH, the atmosphere and oceans reverse roles, with the atmosphere transporting heat southward while the oceans transport heat northward. Aside from the magnitude of the cross-equatorial heat flux, the AIE case is almost a mirror opposite of the LLGHG case for both atmospheric and oceanic transports, supported by correlation coefficients of $r^2 = 0.87$ for the atmospheric heat transports and $r^2 = 0.81$ for oceanic heat transports.

The difference in aerosol direct and indirect oceanic responses may be due to the spatial distributions of the two forcings differing in terms of land–ocean contrast. Marine clouds, which are prevalent, enhance the indirect effect, but mask DRF over the ocean. Thus, in this sense, AIE may be more capable of forcing the ocean than SUL DRF, thus giving rise to different oceanic responses.

The SUL and AER results are consistent with the findings of Cai et al. (2006), which show northward cross-equatorial heat flow in the oceans when the NH is dominated by cooling aerosols. There is therefore a consistency emerging from different models regarding the robust influence of aerosols on ocean heat transport. The cross-equatorial heat flux attributable to interhemispherically asymmetrical forcings has also been discussed before (Ramaswamy and Chen 1997; Kang et al. 2008; Ming and Ramaswamy 2011; Friedman et al. 2013), mainly in the context of an atmospheric model being coupled to a mixed-layer ocean model.

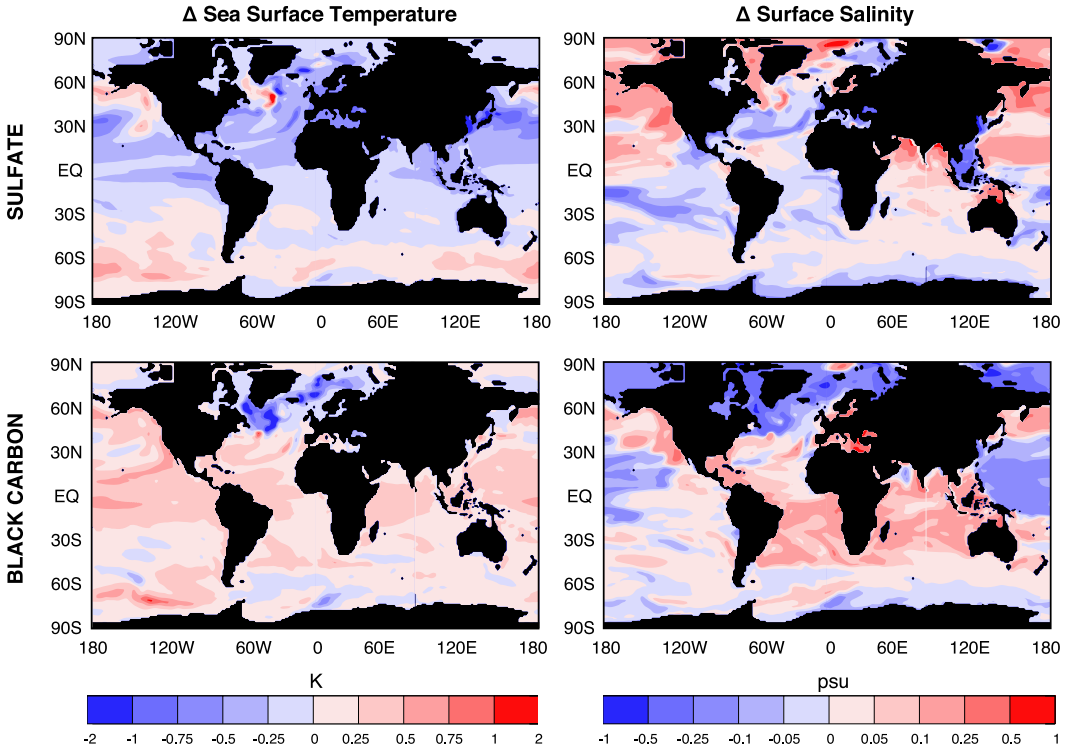

FIG. 7. Annual mean responses in (left) SST and (right) salinity from isolated forcing scenarios, computed as the difference between PI (1861–80) and PD (1981–2000) conditions.

The significance of using a coupled climate model with a full ocean is demonstrated in this study, because it reveals the importance of the ocean in redistributing heat in addition to the atmosphere, especially for aerosol forcings. This cannot be deduced using a mixed-layer ocean model. Furthermore, because the magnitudes of the heat transport responses for the aerosols are similar for both the atmospheric and oceanic components, the ocean in fact is more perturbed than the atmosphere. This is because in the mean climate state, the atmosphere transports 2–3 times more heat than the ocean outside of the tropics (Fig. 5) (e.g., Marshall and Plumb 2008).

c. *Oceanic responses*

To take advantage of the full ocean model, we calculate responses of additional ocean variables (sea surface temperature and surface salinity) to scattering and absorbing aerosol isolated forcings. We restrict considerations to the SUL and BC scenarios. Figure 7 shows the spatial responses in SST and surface salinity for SUL and BC isolated forcing scenarios.

1) SEA SURFACE TEMPERATURE

SUL and BC generally yield opposite SST changes (ΔSST), especially in the NH. The strongest cooling responses to SUL are found in the NH, consistent with Williams et al. (2001). BC yields warming responses in the tropics and subtropics, but with a stronger response in the NH. A notable exception is the Labrador Sea, which warms in SUL but cools in BC. This is because the overall cooling in SUL (warming in BC) leads to a strengthening (weakening) of the Atlantic meridional overturning circulation (AMOC). The physical mechanisms are similar to those discussed in the context of global warming (increased input of freshwater) (e.g., Manabe and Stouffer 2007).

Rotstayn et al. (2000) use an atmospheric model with prescribed SSTs to show that equatorial precipitation shifts southward in the presence of the aerosol indirect effect, and hypothesize that it is caused by the interhemispheric asymmetry in the cooling of SSTs. Similarly, Williams et al. (2001) use an atmospheric model with a slab ocean to show that cooling in the NH high latitudes from the aerosol indirect effect yields an SST gradient that causes a southward shift in the ITCZ. Our analysis of changes in ΔSST from the SUL experiment, with the inclusion of a full ocean, supports these results of how negative forcings predominantly in the NH impact SST. We find that the SSTs in the NH are cooled more so than that of the SH (Fig. 7), introducing a cooling gradient that can influence precipitation.

2) SURFACE SALINITY

Surface salinity is related to the net flux of precipitation and evaporation. For example, if precipitation increases in a region, the ocean surface will become fresher, and salinity will decrease. If, on the other hand, precipitation decreases, the ocean surface salinity will increase. Thus, any change in the surface salinity can be thought of, to the first order, as driven by the net change in precipitation minus evaporation ($P - E$). Since precipitation has more structure than evaporation, the former is more important for determining the spatial distribution of the simulated surface salinity change.

The main precipitation changes for SUL and BC are found in the tropics, where SUL shifts the ITCZ southward and BC shifts the ITCZ northward (Fig. 3). SUL zonal ΔP therefore shows an increase in precipitation south of the equator and a decrease in precipitation north of the equator. Figure 7 shows that, for SUL, the surface ocean salinity indeed responds with a decrease in salinity south of the equator (seen in the Pacific and Atlantic Ocean basins) and an increase in salinity north of the equator (seen in the Pacific and Indian Ocean basins). BC yields the opposite results. BC zonal ΔP shows a decrease in precipitation south of the equator and an increase in precipitation north of the equator (Fig. 3). The surface ocean salinity responds with an increase in salinity south of the equator (seen in the Atlantic and Indian Ocean basins) and a decrease in salinity north of the equator (seen in the Pacific Ocean basin) (Fig. 7).

Opposing scattering and absorbing aerosols' salinity responses that correspond to precipitation responses are also found in the Arctic. SUL increases the salinity in the Arctic, whereas BC decreases the salinity in the Arctic (Fig. 7). This is a reflection of the decreased (increased) precipitation in the Arctic for SUL (BC), shown in Fig. 3. Further, salty bodies of water in the subtropics—such as the Mediterranean Sea—are particularly influenced by the aerosol forcings. SUL decreases the salinity in these seas around 0.5 psu, while BC considerably increases the salinity by almost 1 psu (mean salinity climatology is around 40 psu in the Mediterranean Sea). A thermodynamic argument put forward in Held and Soden (2006) indicates that $P - E$ would decrease in the subtropics in response to global warming. As shown in Ming and Ramaswamy (2011), aerosol cooling would lead to the opposite effect, namely an increase in $P - E$ in the subtropics. The salinity results appear to be consistent, at least qualitatively, with the thermodynamic control of $P - E$.

4. Conclusions

This study has investigated the preindustrial to present-day thermal, hydrological, and dynamical atmospheric and oceanic responses to a comprehensive set of isolated forcing simulations, which enable the individual effects of scattering and absorbing aerosols (and the indirect effect) to be compared within the same model and also to the effects of long-lived greenhouse gases. While climate responses to aerosols have been analyzed in previous studies to varying degrees, the majority of earlier work has been done with atmospheric models coupled to simple slab ocean models. We therefore employ a coupled ocean–atmosphere model to parse out atmospheric and oceanic responses to scattering and absorbing aerosols. One unique aspect of this study is focusing separately on the responses of atmospheric and oceanic meridional heat transport to aerosol forcing.

The analysis reveals the particular importance of 1) the sign of the radiative forcing, 2) the spatial distribution of the forcing, and 3) the response of the ocean in addition to the atmosphere. We find that aerosol climate response patterns (e.g., cross-equatorial precipitation, circulation, and heat transport) are governed by the sign and magnitude of the aerosol forcing and its interhemispheric forcing asymmetry, introducing a consistent anticorrelation in responses amongst scattering and absorbing aerosols, and unique responses specific to aerosols that differ from that of LLGHGs.

Sulfate and black carbon—two prominent anthropogenic scattering and absorbing aerosol species, respectively—have similar forcing distributions with opposite signs, and have consistently opposite climate responses. Sulfate (black carbon) is generally cooling (warming), shifts the ITCZ southward (northward), weakens (strengthens) the summertime Hadley cell, strengthens (weakens) the wintertime Hadley cell, transports heat northward (southward) across the equator, and strengthens (weakens) the AMOC. Using the model simulations, we highlight a strong evidence of a contrast in equatorial precipitation, circulation, vertical velocity, atmospheric and oceanic heat transport, sea surface temperature, and salinity responses to scattering and absorbing aerosols. The additional aerosol cases employed (scattering for AIE and OC, and absorbing for BCL) corroborate these findings.

It is important to note, however, that black carbon warming of the surface versus radiative heating of the atmosphere yields opposing global mean precipitation responses that are partially offsetting, dependent on the vertical profile of the absorbing aerosols. Black carbon at lower elevations increases surface temperature and precipitation as compared to black carbon at higher elevations. While hydrological responses to black carbon forcings are weakened by opposing processes in the atmosphere and at the surface and are to some extent dependent on the aerosol vertical profile, zonal mean

responses still mirror that of sulfate. The conclusion that thermal and hydrological responses to black carbon are sensitive to the elevation of the aerosols is also demonstrated by the modeling study of Ban-Weiss et al. (2012). This sensitivity for black carbon aerosol direct forcing does not arise for the scattering sulfate aerosol.

While LLGHG responses mostly appear to mirror responses to the aerosol indirect effect—which we attribute to opposite forcing signs and an enhancement of the AIE forcing over oceans—there are key differences in responses to LLGHGs compared to the aerosol responses, resulting from the different spatial distributions of forcing. LLGHGs are well mixed, yielding radiative forcings that are globally uniform with little interhemispheric asymmetry. Aerosol radiative forcings are asymmetrically distributed, and mainly concentrated in the Northern Hemisphere. Comparing response patterns from all of the aerosol configuration cases to that from the LLGHG case highlights the significance of the interhemispheric aerosol forcing asymmetry, and allows for detection of a distinct aerosol signature in climate responses.

For precipitation, LLGHG responses are fairly symmetrical about the equator, whereas aerosols increase precipitation in the tropics of one hemisphere and decrease precipitation in the tropics of the other hemisphere. For atmospheric circulation, LLGHGs weakly influence Hadley cell circulation in the annual mean, although there is some evidence of opposing circulations on each side of the equator that likely relates to the typical ''enhanced equatorial warming'' (Liu et al. 2005). On the other hand, aerosols considerably strengthen the ascending branch of circulation in one hemisphere, and weaken the ascending branch in the other hemisphere. For heat transport, LLGHGs do not yield a significant cross-equatorial energy flux, whereas aerosols force both the atmosphere and ocean to redistribute heat across the equator. The general characteristics of the responses to the globally symmetric and interhemispherically asymmetric forcings follow that studied earlier in different contexts (Manabe and Broccoli 1985; Taylor and Penner 1994; Ramaswamy and Chen 1997; Rotstayn et al. 2000; Chiang and Friedman 2012; Friedman et al. 2013). Further, the contrast in the responses between the LLGHGs and aerosols has a consistency with the Last Glacial Maximum's NH ice sheet responses on the global climate studied by Manabe and Broccoli (1985).

Although aerosols distinctly affect the climate in different ways than LLGHGs—attributed to the strong interhemispheric forcing asymmetry exhibited by aerosols—detecting aerosol's contribution to climate change is difficult because the individual forcings and responses of aerosol components are opposite and operating simultaneously. Indeed, the total aerosol DRF scenario (AER) yields climate responses that generally follow the characteristics of sulfate (SUL), but are considerably weakened by the contribution of black carbon (BC) responses. Therefore, it is likely that the canceling out of strong individual aerosol climate responses is concealing the actual attribution of individual aerosols to climate change.

There is a broad agreement in the commonality of the spatial pattern of the LLGHGs' and aerosols' temperature and precipitation responses between Xie et al. (2013) and our simulations. However, the dipole-like structure of the zonal-mean precipitation responses just north and south of the equator for the aerosol cases appears to be more pronounced in our results. The differing features of the dipole-like structure around the equator in precipitation arising for aerosols and less so for the LLGHG case are likely dependent on the aerosol characteristics in the model simulations. The two modeling studies differ in their aerosol representations, and separate aerosol forcing (absorbing and scattering) runs as performed in this study are needed to infer that the dipole is a physical manifestation.

An additional finding from this study is that oceanic heat transport is greatly perturbed by aerosol forcings, and is perturbed more so than that of the atmosphere. Thus, the climate change problem in terms of heat transports in each hemisphere can be investigated in completion only by using a coupled global climate model with a full ocean, in contrast to a mixed layer. Using CM2.1, we find that there is a significant cross-equatorial energy flux established in both the atmosphere and the ocean from the aerosol forcings, and both the atmosphere and ocean are transporting heat across the equator in the same direction. Our results are consistent with the findings of Cowan and Cai (2013), which show a substantial aerosol influence on ocean heat redistribution, although they also found that the effect of Asian aerosols was small.

Further investigation of ocean responses to aerosols shows that scattering and absorbing aerosols perturb sea surface temperature and surface salinity in opposite ways. Aerosol influence on the sea surface temperature provides insight into the strengthening or weakening of the Atlantic meridional overturning circulation, with the aerosol influence on salinity accompanying approximately the precipitation responses.

Comparisons to previous studies for aerosol effects on dynamical properties are limited (e.g., Roberts and Jones 2004; Frieler et al. 2011). While most studies focus on climate responses to greenhouse gases and/or aerosols (e.g., Frierson and Hwang 2012; Cowan and Cai 2013), few (e.g., Yoshimori and Broccoli 2008) isolate the

individual aerosol responses in the climate system, and especially relating to the circulation features. Randles and Ramaswamy (2008) discuss the contrast in responses to the presence of scattering versus absorbing aerosols in the Asian region, showing that changes in temperature, cloud distributions at different heights, and precipitation all depend on the sign of the aerosol forcing. However, the results were in the context of an atmospheric general circulation model forced by prescribed sea surface temperature.

Yoshimori and Broccoli (2008) and Ming and Ramaswamy (2011) analyze thermal, hydrological, and dynamical responses to aerosol and greenhouse gas forcings using a mixed-layer ocean version of the GFDL atmospheric model, version 2.1 (AM2.1; the atmospheric component of CM2.1). We find that the major differences in responses (from the full ocean) occur in the Southern Ocean temperature response and, as expected, the ability to partition the total heat transport response between the atmosphere and ocean. Shifts in the ITCZ and responses in the meridional streamfunction remain consistent. This study, performed with a well-recognized coupled climate model with a full ocean, is an initial step toward understanding how different types of aerosol forcings (scattering, absorbing, and indirect effects) influence dynamical climate features in both the atmosphere and ocean.

We use a simplified treatment of aerosol distributions and optics as a means to isolate climate responses from scattering versus absorbing aerosols. Mixing state assumptions (e.g., sulfate and black carbon existing as internal mixtures), in particular, can significantly affect climate responses. Chung and Seinfeld (2005) find that the global mean temperature response from black carbon, when internally mixed with sulfate, almost doubles. An extrapolation to cases when aerosols are considered as internal mixtures could yield a first-order estimate by considering a linear sum of the sulfate DRF and black carbon DRF cases. Nonlinearity is an issue, however, because the addition of forcings yields such an effect in the case of mixtures (Ocko et al. 2012), and therefore the responses would as well. However, a linear aggregation would lead to the conclusion that the circulation and heat transport responses would be intermediate between the black carbon and sulfate. A more complex problem would arise when the full gamut of the aerosol–cloud interaction (Denman et al. 2007) is considered, with a likely considerable sensitivity to cloud–aerosol microphysics treatments and other model parameterizations (Golaz et al. 2011). Lastly, our results are model dependent. Studies have shown that the tropical response to interhemispherically asymmetrical forcings is dependent on model parameterizations and model-simulated cloud feedbacks (e.g., Kang et al. 2008).

Acknowledgments. Ilissa B. Ocko was supported by the National Science Foundation Graduate Research Fellowship under Grant DGE 0646086. We thank Dan Schwarzkopf and Geeta Persad for providing several forcing estimates, David Paynter for suggestions and comments, Gabriel Vecchi for reading an earlier draft of the manuscript, and three anonymous reviewers for helpful comments.

REFERENCES

Ackerley, D., B. B. Booth, S. H. Knight, E. J. Highwood, D. J. Frame, M. R. Allen, and D. P. Rowell, 2011: Sensitivity of twentieth-century Sahel rainfall to sulfate aerosol and CO_2 forcing. *J. Climate,* **24,** 4999–5014, doi:10.1175/JCLI-D-11-00019.1.

Anderson, J. L., and Coauthors, 2004: The new GFDL global atmosphere and land model AM2-LM2: Evaluation with prescribed SST simulations. *J. Climate,* **17,** 4641–4673, doi:10.1175/JCLI-3223.1.

Andrews, T., P. M. Forster, O. Boucher, N. Bellouin, and A. Jones, 2010: Precipitation, radiative forcing and global temperature change. *Geophys. Res. Lett.,* **37,** L14701, doi:10.1029/2010GL043991.

Ban-Weiss, G. A., L. Cao, G. Bala, and K. Caldeira, 2012: Dependence of climate forcing and response on the altitude of black carbon aerosols. *Climate Dyn.,* **38,** 897–911, doi:10.1007/s00382-011-1052-y.

Bollasina, M. A., Y. Ming, and V. Ramaswamy, 2011: Anthropogenic aerosols and the weakening of the South Asian summer monsoon. *Science,* **334,** 502–505, doi:10.1126/science.1204994.

Cai, W., D. Bi, J. Church, T. Cowan, M. Dix, and L. Rotstayn, 2006: Pan-oceanic response to increasing anthropogenic aerosols: Impacts on the Southern Hemisphere oceanic circulation. *Geophys. Res. Lett.,* **33,** L21707, doi:10.1029/2006GL027513.

Chiang, J. C., and A. R. Friedman, 2012: Extratropical cooling, interhemispheric thermal gradients, and tropical climate change. *Annu. Rev. Earth Planet. Sci.,* **40,** 383–412, doi:10.1146/annurev-earth-042711-105545.

Chung, C. E., V. Ramaswamy, and J. T. Kiehl, 2002: Effects of the South Asian absorbing haze on the northeast monsoon and surface–air heat exchange. *J. Climate,* **15,** 2462–2476, doi:10.1175/1520-0442(2002)015<2462:EOTSAA>2.0.CO;2.

Chung, S. H., and J. H. Seinfeld, 2005: Climate response of direct radiative forcing of anthropogenic black carbon. *J. Geophys. Res.,* **110,** D11102, doi:10.1029/2004JD005441.

Cooke, W. F., C. Liousse, H. Cachier, and J. Feichter, 1999: Construction of a 1° × 1° fossil fuel emission dataset for carbonaceous aerosol and implementation and radiative impact in the ECHAM-4 model. *J. Geophys. Res.,* **104,** 22 137–22 162, doi:10.1029/1999JD900187.

Cowan, T., and W. Cai, 2013: The response of the large-scale ocean circulation to 20th century Asian and non-Asian aerosols. *Geophys. Res. Lett.,* **40,** 2761–2767, doi:10.1002/grl.50587.

Delworth, T. L., and Coauthors, 2006: GFDL's CM2 global coupled climate models. Part I: Formulation and simulation characteristics. *J. Climate,* **19,** 643–674, doi:10.1175/JCLI3629.1.

Denman, K. L., and Coauthors, 2007: Couplings between changes in the climate system and biogeochemistry. *Climate Change 2007: The Physical Science Basis,* S. Solomon et al., Eds., Cambridge University Press, 499–587.

Erlick, C., V. Ramaswamy, and L. M. Russell, 2006: Differing regional responses to a perturbation in solar cloud absorption in the SKYHI general circulation model. *J. Geophys. Res.,* **111,** D06204, doi:10.1029/2005JD006491.

Feichter, J., E. Roeckner, U. Lohmann, and D. Liepert, 2004: Nonlinear aspects of the climate response to greenhouse gas and aerosol forcing. *J. Climate,* **17,** 2384–2398, doi:10.1175/1520-0442(2004)017<2384:NAOTCR>2.0.CO;2.

Forster, P., and Coauthors, 2007: Changes in atmospheric constituents and in radiative forcing. *Climate Change 2007: The Physical Science Basis,* S. Solomon et al., Eds., Cambridge University Press, 129–234.

Freidenreich, S. M., and V. Ramaswamy, 1999: A new multiple-band solar radiative parameterization for general circulation models. *J. Geophys. Res.,* **104,** 31 389–31 409, doi:10.1029/1999JD900456.

Friedman, A. R., Y.-T. Hwang, J. C. Chiang, and D. M. Frierson, 2013: Interhemispheric temperature asymmetry over the twentieth century and in future projections. *J. Climate,* **26,** 5419–5433, doi:10.1175/JCLI-D-12-00525.1.

Frieler, K., M. Meinshausen, T. Schneider von Deimling, T. Andrews, and P. Forster, 2011: Changes in global-mean precipitation in response to warming, greenhouse gas forcing and black carbon. *Geophys. Res. Lett.,* **38,** L04702, doi:10.1029/2010GL045953.

Frierson, D. M. W., and Y.-T. Hwang, 2012: Extratropical influence on ITCZ shifts in slab ocean simulations of global warming. *J. Climate,* **25,** 720–733, doi:10.1175/JCLI-D-11-00116.1.

Ginoux, P., L. W. Horowitz, V. Ramaswamy, I. V. Geogdzhayev, B. N. Holben, G. Stenchikov, and X. Tie, 2006: Evaluation of aerosol distribution and optical depth in the Geophysical Fluid Dynamics Laboratory coupled model CM2.1 for present climate. *J. Geophys. Res.,* **111,** D22210, doi:10.1029/2005JD006707.

Golaz, J.-C., M. Salzmann, L. J. Donner, L. W. Horowitz, Y. Ming, and M. Zhao, 2011: Sensitivity of the aerosol indirect effect to subgrid variability in the cloud parameterization of the GFDL atmosphere general circulation model AM3. *J. Climate,* **24,** doi:10.1175/2010JCLI3945.1.

Hansen, J., M. Sato, A. Lacis, R. Ruedy, I. Tegen, and E. Matthews, 1998: Climate forcings in the Industrial era. *Proc. Natl. Acad. Sci. USA,* **95,** 12 753–12 758, doi:10.1073/pnas.95.22.12753.

Haywood, J. M., and V. Ramaswamy, 1998: Global sensitivity studies of the direct radiative forcing due to anthropogenic sulfate and black carbon aerosols. *J. Geophys. Res.,* **103,** 6043–6058, doi:10.1029/97JD03426.

Held, I. M., 2001: The partitioning of the poleward energy transport between the tropical ocean and atmosphere. *J. Atmos. Sci.,* **58,** 943–948, doi:10.1175/1520-0469(2001)058<0943:TPOTPE>2.0.CO;2.

——, and B. J. Soden, 2006: Robust responses of the hydrological cycle to global warming. *J. Climate,* **19,** 5686–5699, doi:10.1175/JCLI3990.1.

Hill, S., Y. Ming, and I. M. Held, 2014: Mechanisms of forced tropical meridional energy flux change. *J. Climate,* doi:10.1175/JCLI-D-14-00165.1, in press.

Horowitz, L. W., 2006: Past, present, and future concentrations of tropospheric ozone and aerosols: Methodology, ozone evaluation, and sensitivity to aerosol wet removal. *J. Geophys. Res.,* **111,** D22211, doi:10.1029/2005JD006937.

Hunke, E. C., and J. K. Dukowicz, 1997: An elastic–viscous–plastic model for sea ice dynamics. *J. Phys. Oceanogr.,* **27,** 1849–1867, doi:10.1175/1520-0485(1997)027<1849:AEVPMF>2.0.CO;2.

Hwang, Y. T., D. M. Frierson, and S. M. Kang, 2013: Anthropogenic sulfate aerosol and the southward shift of tropical precipitation in the late 20th century. *Geophys. Res. Lett.,* **40,** 2845–2850, doi:10.1002/grl.50502.

Jones, A., J. M. Haywood, and O. Boucher, 2007: Aerosol forcing, climate response and climate sensitivity in the Hadley Centre climate model. *J. Geophys. Res.,* **112,** D20211, doi:10.1029/2007JD008688.

Kang, S. M., I. M. Held, D. M. W. Frierson, and M. Zhao, 2008: The response of the ITCZ to extratropical thermal forcing: Idealized slab-ocean experiments with a GCM. *J. Climate,* **21,** 3521–3532, doi:10.1175/2007JCLI2146.1.

Knutson, T. R., and Coauthors, 2006: Assessment of twentieth-century regional surface temperature trends using the GFDL CM2 coupled models. *J. Climate,* **19,** 1624–1651, doi:10.1175/JCLI3709.1.

Koch, D., and Coauthors, 2009: Evaluation of black carbon estimations in global aerosol models. *Atmos. Chem. Phys.,* **9,** 9001–9026, doi:10.5194/acp-9-9001-2009.

Liu, Z., S. Vavrus, F. He, N. Wen, and Y. Zhong, 2005: Rethinking tropical ocean response to global warming: The enhanced equatorial warming. *J. Climate,* **18,** 4684–4700, doi:10.1175/JCLI3579.1.

Lohmann, U., and J. Feichter, 2005: Global indirect aerosol effects: A review. *Atmos. Chem. Phys.,* **5,** 715–737, doi:10.5194/acp-5-715-2005.

Lu, J., and B. Zhao, 2012: The role of oceanic feedback in the climate response to doubling CO_2. *J. Climate,* **25,** 7544–7563, doi:10.1175/JCLI-D-11-00712.1.

Mahajan, S., K. J. Evans, J. J. Hack, and J. E. Truesdale, 2013: Linearity of climate response to increases in black carbon aerosols. *J. Climate,* **26,** 8223–8237, doi:10.1175/JCLI-D-12-00715.1.

Manabe, S., and A. J. Broccoli, 1985: The influence of continental ice sheets on the climate of an ice age. *J. Geophys. Res.,* **90,** 2167–2190, doi:10.1029/JD090iD01p02167.

——, and R. J. Stouffer, 2007: Role of ocean in global warming. *J. Meteor. Soc. Japan,* **85B,** 385–403, doi:10.2151/jmsj.85B.385.

Marshall, J., and R. A. Plumb, 2008: *Atmosphere, Ocean, and Climate Dynamics: An Introductory Text.* Elsevier, 344 pp.

Meehl, G. A., J. M. Arblaster, and W. D. Collins, 2008: Effects of black carbon aerosols on the Indian monsoon. *J. Climate,* **21,** 2869–2882, doi:10.1175/2007JCLI1777.1.

Ming, Y., and V. Ramaswamy, 2009: Nonlinear climate and hydrological responses to aerosol effects. *J. Climate,* **22,** 1329–1339, doi:10.1175/2008JCLI2362.1.

——, and ——, 2011: A model investigation of aerosol-induced changes in tropical circulation. *J. Climate,* **24,** 5125–5133, doi:10.1175/2011JCLI4108.1.

——, ——, P. Ginoux, L. W. Horowitz, and L. M. Russell, 2005: Geophysical Fluid Dynamics Laboratory general circulation model investigation of the indirect radiative effects of anthropogenic sulfate aerosol. *J. Geophys. Res.,* **110,** D22206, doi:10.1029/2005JD006161.

——, ——, and G. Persad, 2010: Two opposing effects of absorbing aerosols on global-mean precipitation. *Geophys. Res. Lett.,* **37,** L13701, doi:10.1029/2010GL042895.

Ocko, I. B., V. Ramaswamy, P. Ginoux, Y. Ming, and L. W. Horowitz, 2012: Sensitivity of scattering and absorbing aerosol direct radiative forcing to physical climate factors. *J. Geophys. Res.,* **117,** D20203, doi:10.1029/2012JD018019.

Olivier, J. G. J., and Coauthors, 1996: Description of EDGAR version 2.0: A set of global emission inventories of greenhouse gases and ozone depleting substances for all anthropogenic and most natural sources on a per country basis and on a 1×1 degree grid. RIVM Rep. 771060 002 TNO-MEP Rep.

R96/119, National Institute for Public Health and the Environment, Bilthoven, Netherlands, 171 pp.

Ramanathan, V., and G. Carmichael, 2008: Global and regional climate changes due to black carbon. *Nat. Geosci.,* **1,** 221–227, doi:10.1038/ngeo156.

——, P. J. Crutzen, J. T. Kiehl, and D. Rosenfeld, 2001: Aerosols, climate, and the hydrological cycle. *Science,* **294,** 2119–2124, doi:10.1126/science.1064034.

Ramaswamy, V., and C.-T. Chen, 1997: Climate forcing–response relationships for greenhouse and shortwave radiative perturbations. *Geophys. Res. Lett.,* **24,** 667–670, doi:10.1029/97GL00253.

Randles, C. A., and V. Ramaswamy, 2008: Absorbing aerosols over Asia: A Geophysical Fluid Dynamics Laboratory general circulation model sensitivity study of model response to aerosol optical depth and aerosol absorption. *J. Geophys. Res.,* **113,** D21203, doi:10.1029/2008JD010140.

Reichler, T., and J. Kim, 2008: How well do coupled models simulate today's climate? *Bull. Amer. Meteor. Soc.,* **89,** 303–311, doi:10.1175/BAMS-89-3-303.

Roberts, D. L., and A. Jones, 2004: Climate sensitivity to black carbon aerosol from fossil fuel combustion. *J. Geophys. Res.,* **109,** D16202, doi:10.1029/2004JD004676.

Rotstayn, L. D., and U. Lohmann, 2002: Tropical rainfall trends and the indirect aerosol effect. *J. Climate,* **15,** 2103–2116, doi:10.1175/1520-0442(2002)015<2103:TRTATI>2.0.CO;2.

——, B. F. Ryan, and J. E. Penner, 2000: Precipitation changes in a GCM resulting from the indirect effects of anthropogenic aerosols. *Geophys. Res. Lett.,* **27,** 3045–3048, doi:10.1029/2000GL011737.

——, S. J. Jeffrey, M. A. Collier, S. M. Dravitzki, A. C. Hirst, J. I. Syktus, and K. K. Wong, 2012: Aerosol- and greenhouse gas-induced changes in summer rainfall and circulation in the Australasian region: A study using single-forcing climate simulations. *Atmos. Chem. Phys.,* **12,** 6377–6404, doi:10.5194/acp-12-6377-2012.

Santer, B. D., T. M. L. Wigley, J. S. Boyle, D. J. Gaffen, J. J. Hnilo, D. Nychka, D. E. Parker, and K. E. Taylor, 2000: Statistical significance of trends and trend differences in layer-average atmospheric temperature time series. *J. Geophys. Res.,* **105,** 7337–7356, doi:10.1029/1999JD901105.

Schwarzkopf, M. D., and V. Ramaswamy, 1999: Radiative edicts of CH_2, N_2O, halocarbons and the foreign-broadened H_2O continuum: A GCM experiment. *J. Geophys. Res.,* **104,** 9467–9488, doi:10.1029/1999JD900003.

Shindell, D., M. Schulz, Y. Ming, T. Takemura, G. Faluvegi, and V. Ramaswamy, 2010: Spatial scales of climate response to inhomogeneous radiative forcing. *J. Geophys. Res.,* **115,** D19110, doi:10.1029/2010JD014108.

Solomon, S., D. Qin, M. Manning, Z. Chen, M. Marquis, K. Averyt, M. M. B. Tignor, and H. L. Miller Jr., 2007: *Climate Change 2007: The Physical Science Basis.* Cambridge University Press, 996 pp.

Stouffer, R. J., S. Manabe, and K. Bryan, 1989: Interhemispheric asymmetry in climate response to a gradual increase of atmospheric CO_2. *Nature,* **342,** 660–662, doi:10.1038/342660a0.

——, A. J. Weaver, and M. Eby, 2004: A method for obtaining pre-twentieth century initial conditions for use in climate change studies. *Climate Dyn.,* **23,** 327–339, doi:10.1007/s00382-004-0446-5.

Takemura, T., T. Nozawa, S. Emori, T. Y. Nakajima, and T. Nakajima, 2005: Simulation of climate response to aerosol direct and indirect effects with aerosol transport-radiation model. *J. Geophys. Res.,* **110,** D02202, doi:10.1029/2004JD005029.

Tang, I. N., and H. R. Munkelwitz, 1994: Water activities, densities, and refractive indices of aqueous sulfates and sodium nitrate droplets of atmospheric importance. *J. Geophys. Res.,* **99,** 18 801–18 808, doi:10.1029/94JD01345.

Taylor, K. E., and J. E. Penner, 1994: Response of the climate system to atmospheric aerosols and greenhouse gases. *Nature,* **369,** 734–737, doi:10.1038/369734a0.

Tie, X., and Coauthors, 2005: Assessment of the global impact of aerosols on tropospheric oxidants. *J. Geophys. Res.,* **110,** D03204, doi:10.1029/2004JD005359.

van Aardenne, J. A., F. J. Dentener, G. J. Olivier, C. G. M. Klein Goldewijk, and J. Lelieveld, 2001: A $1° \times 1°$ resolution data set of historical anthropogenic trace gas emissions for the period 1890–1990. *Global Biogeochem. Cycles,* **15,** 909–928, doi:10.1029/2000GB001265.

Wang, C., 2004: A modeling study on the climate impacts of black carbon aerosols. *J. Geophys. Res.,* **109,** D03106, doi:10.1029/2003JD004084.

Williams, K. D., A. Jones, D. L. Roberts, C. A. Senior, and M. J. Woodage, 2001: The response of the climate system to the indirect effects of anthropogenic sulfate aerosol. *Climate Dyn.,* **17,** 845–856, doi:10.1007/s003820100150.

Winton, M., 2000: A reformulated three-layer sea ice model. *J. Atmos. Oceanic Technol.,* **17,** 525–531, doi:10.1175/1520-0426(2000)017<0525:ARTLSI>2.0.CO;2.

Xie, S. P., B. Lu, and B. Xiang, 2013: Similar spatial patterns of climate responses to aerosol and greenhouse gas changes. *Nat. Geosci.,* **6,** 828–832, doi:10.1038/ngeo1931.

Yoshimori, M., and A. J. Broccoli, 2008: Equilibrium response of an atmosphere–mixed layer ocean model to different radiative forcing agents: Global and zonal mean response. *J. Climate,* **21,** 4399–4423, doi:10.1175/2008JCLI2172.1.